Tetravalent SARS-CoV-2 Neutralizing Antibodies Show Enhanced Potency and Resistance to Escape Mutations

Shane Miersch[1, 8], Zhijie Li[2, 8], Reza Saberianfar[1], Mart Ustav[3], Levi Blazer[1], Chao Chen[1], Wei Ye[1], Alia Pavlenco[1], Suryasree Subramania[1], Serena Singh[1], Lynda Ploder[1], Safder Ganaie[4], Daisy Leung[4], Rita E. Chen[4], James Brett Case[4], Guiseppe Novelli[5], Giulia Matusali[6], Francesca Colavita[6], Maria R. Copabianchi[6], Suresh Jain[7], J.B. Gupta[7], Gaya Amarasinghe[4], Michael Diamond[4], James Rini[2,*], Sachdev S. Sidhu[1,*]

Affiliations

1 - The Donnelly Centre, University of Toronto, Toronto, Canada

2 - Department of Biochemistry, University of Toronto, Toronto, Canada

3 - Icosagen, Õssu, Estonia

4 - Department of Medicine, Washington University School of Medicine, St. Louis, MO, USA

5 - Department of Biomedicine and Prevention, Tor Vergata University of Rome, 00133, Rome, Italy

6 - Laboratory of Virology, National Institute for Infectious Diseases "L. Spallanzani" IRCCS, Rome, Italy

7 - Virna Therapeutics, West Roxbury, MA, USA

8 - The authors contributed equally

*** - Corresponding author**

Corresponding authors email: james.rini@utoronto.ca and sachdev.sidhu@utoronto.ca

ABSTRACT

Recombinant neutralizing antibodies (nAbs) derived from recovered patients have proven to be effective therapeutics for COVID-19. Here, we describe the use of advanced protein engineering and modular design principles to develop tetravalent synthetic nAbs that mimic the multi-valency exhibited by IgA molecules, which are especially effective natural inhibitors of viral disease. At the same time, these nAbs display high affinity and modularity typical of IgG molecules, which are the preferred format for drugs. We show that highly specific tetravalent nAbs can be produced at large scale and possess stability and specificity comparable to approved antibody drugs. Moreover, structural studies reveal that the best nAb targets the host receptor binding site of the virus spike protein, and thus, its tetravalent version can block virus infection with a potency that exceeds that of the bivalent IgG by an order of magnitude. Design principles defined here can be readily applied to any antibody drug, including IgGs that are showing efficacy in clinical trials. Thus, our results present a general framework to develop potent antiviral therapies against COVID-19, and the strategy can be readily deployed in response to future pathogenic threats.

44 **INTRODUCTION**

45 As of October 30, 2020, the ongoing COVID-19 viral pandemic has tallied more than
46 44,000,000 confirmed infections and caused over 1,100,000 deaths (www.who.int). Moreover,
47 the highly infectious nature of the disease has imposed severe economic hardship across the
48 world due to the need for social distancing and lockdown measures. Despite intensive global
49 efforts, no effective vaccines have yet been approved, and a number of repurposed drugs have
50 shown only limited or uncertain efficacy[1,2]. Thus, there is an urgent need for potent targeted
51 therapies that can inhibit the SARS-CoV-2 virus directly, by blocking either its entry into host cells
52 or its replication and subsequent release from cells.

53 Several lines of evidence suggest that SARS-CoV-2 neutralizing antibodies (nAbs) that bind
54 directly to the virus and inhibit entry into host cells have therapeutic potential. First, many
55 infected individuals either remain asymptomatic or recover rapidly with only minimal symptoms,
56 and the plasma from these patients usually contains nAbs[3,4]. Second, transfer of plasma
57 containing nAbs from convalescent patients to symptomatic patients has been beneficial in some
58 cases[5–7]. Third, recombinant nAbs that inhibit the interaction between SARS-CoV-2 and host cells
59 confer protection in cell-based assays and animal models[8,9], and efficacy has also been observed
60 for nAbs targeting the related coronaviruses SARS-CoV[10–12] and MERS[13]. Consequently, a number
61 of nAbs have entered clinical trials as post-infection treatment of COVID-19 associated with SARS-
62 CoV-2 (Clinicaltrials.gov - NCT04452318, NCT04497987).

63 SARS-CoV-2 virions contain 25-100 glycosylated spike (S) proteins that protrude from the
64 virus surface[14,15]. Surface-associated S proteins bind to angiotensin-converting enzyme 2 (ACE2)
65 to mediate host cell entry[16]. The S protein contains two subunits (S1 and S2) and forms a
66 homotrimer. The receptor binding domain (RBD), located in the C-terminal region of the S1
67 subunit, recognizes ACE2 on host cells; binding facilitates cleavage of the S2 subunit by cell-
68 surface proteases, which in turn promotes fusion and internalization of the virus[16]. The most
69 potent nAbs against both SARS-CoV-2 and SARS-CoV block ACE2 through direct competition for
70 binding to the RBD[17–21]. Consequently, we focused our efforts on developing Abs that bound to
71 the RBD and competed with ACE2.

72 To date, all clinically advanced candidate nAbs against SARS-CoV-2 infection have been
73 derived by cloning from B-cells of recovered COVID-19 patients or from other natural
74 sources[9,17,19–23]. Here, we applied an alternative strategy using *in vitro* selections with phage-
75 displayed libraries of synthetic Abs built on a single human framework derived from the highly
76 validated drug trastuzumab. This approach enabled the rapid production of high affinity nAbs
77 with properties optimized for drug development. Moreover, the use of a highly stable framework
78 enabled facile and modular design of ultra-high affinity nAbs in tetravalent formats that retained
79 favorable drug-like properties and exhibited neutralization potencies that greatly exceeded those
80 of the bivalent IgG format. These methods provide a general means to rapidly improve the
81 potency of virtually any nAb targeting SARS-CoV-2 and its relatives, and thus, our strategy can be
82 applied to improve COVID-19 therapies and can be adapted in response to future pathogenic
83 threats.
84
85

86 **RESULTS**

87 **Engineering of anti-RBD Fabs and IgGs**

88 Using a phage-displayed human antigen-binding fragment (Fab) library similar to the
89 highly validated library F[24], we performed four rounds of selection for binding to the biotinylated
90 RBD of SARS-CoV-2 immobilized on streptavidin-coated plates. Screening of 384 clones for
91 binding to CoV-2 RBD, revealed 348 Fab-phage clones that bound to the RBD but not to
92 streptavidin. Fab-phage were screened by ELISA and those that exhibited >50% loss in binding
93 to RBD in the presence of 200 nM ACE2 were sequenced, revealing 34 unique clones (**Fig. 1A**),
94 deemed to be potential nAbs and converted into the full-length human IgG1 format for
95 purification and functional characterization.

96 To estimate affinities, ELISAs were performed with serial dilutions of IgG protein binding
97 to biotinylated S protein trimer captured with immobilized streptavidin, and these assays showed
98 that three IgGs bound with EC_{50} values in the sub-nanomolar range (**Fig. 1B,C and Table 1**). ELISAs
99 also confirmed that each IgG could partially block the binding of biotinylated ACE2 to immobilized
100 S protein (**Fig. 1D**). Moreover, similar to the highly specific IgG trastuzumab, ELISAs showed that
101 the three IgGs did not bind to seven immobilized proteins that are known to exhibit high non-
102 specific binding to some IgGs, and lack of binding to these proteins has been shown to be
103 predictive of good pharmacokinetics *in vivo* (**Fig. 1E**)[25,26]. We also used biolayer interferometry
104 (BLI) to measure binding kinetics and determine avidities more accurately, and all three
105 antibodies exhibited sub-nanomolar dissociation constants (**Table 1, Fig. S1**), in close accord with
106 the estimates determined by ELISA. IgG 15033 exhibited the highest avidity, which was mainly
107 due to a two- or seven-fold faster on-rate than IgG 15031 or 15032, respectively, and thus, we
108 focused further efforts on this Ab.

109 We took advantage of the precision design of our synthetic Ab library to rapidly improve
110 the affinity of Ab 15033. The synthetic library was designed with tailored diversification of key
111 positions in all three heavy chain complementarity-determining regions (CDRs) and the third CDR
112 of the light chain (CDR-L3). Consequently, we reasoned that the already high affinity of Ab 15033
113 could be further improved by recombining the heavy chain with a library of light chains with naïve
114 diversity in CDR-L3. Following selection for binding to the RBD, the light chain library yielded

115 numerous variants, 17 of which were purified in the IgG format and analyzed by BLI (**Fig. S2**).
116 Several of the variant light chains resulted in IgGs with improved binding compared with IgG
117 15033, and in particular, IgG 15033-7 (**Fig. 1B**) exhibited significantly improved avidity (K_D = 300
118 or 39 pM, respectively) due to an off-rate that was an order of magnitude slower (**Table 1, Fig.**
119 **S2**).
120

121 **Structural analysis of Fabs in complex with the RBD and the S protein**

122 To understand the molecular basis for antagonism of ACE2 binding, we solved the X-ray
123 crystal structures of the SARS-CoV-2 RBD in complex with Fab 15033 or 15033-7 at 3.2 or 3.0 Å
124 resolution, respectively (**Fig. 2A**). As expected, backbone superposition showed that the two
125 complexes were essentially identical (RMSD = 0.17 Å). However, there were differences in side
126 chain interactions due to sequence differences in the CDR-L3 loop, which explained the enhanced
127 affinity of Fab 15033-7 compared with Fab 15033 (**Fig. 2B**). Although the side chains of Tyr^{108L} in
128 Fab 15033 and His^{108L} in Fab 15033-7 both make hydrogen bonds with the side chain of Tyr^{473} in
129 the RBD, the bond mediated by His^{108L} is shorter, and thus, likely to be stronger. Moreover, in
130 Fab 15033-7, the side chain of His^{108L} also makes an intramolecular hydrogen bond with the side
131 chain of Thr^{109L}, which Tyr^{108L} and Arg^{109L} are incapable of making in Fab 15033, and this
132 interaction may stabilize the CDR-L3 loop of Fab 15033-7 in a conformation that is favorable for
133 antigen recognition. Thus, the crystal structures show that the two substitutions in the CDR-L3
134 loop of Fab 15033-7 relative to Fab 15033 act in a cooperative manner to mediate favorable
135 intermolecular contacts with the RBD, and also, intramolecular interactions that stabilize the loop
136 in a conformation that may be better positioned to interact with the RBD.

137 We next analyzed the structures to understand how the Abs could function as antagonists
138 of RBD binding to ACE2. Binding of Fab 15033-7 to the RBD involves an extensive interface, with
139 1130 and 1112 $Å^2$ of surface area buried on the epitope or paratope, respectively, and 59% or
140 41% of the structural paratope is formed by the light or heavy chain, respectively (**Fig. 2C**).
141 Comparison of the Fab and ACE2 epitopes on the RBD revealed extensive overlap, with 79% or
142 69% of the Fab or ACE2 epitope occluded by the other ligand (**Fig. 2C**). Thus, direct steric
143 hinderance explains the blockade of ACE2 binding by Fabs 15033 and 15033-7 (**Fig. 1D**).

144 We also used cryogenic electron microscopy to visualize Fab 15033 in complex with the S
145 protein trimer (**Fig. S3A**). This analysis revealed that all three RBDs in a single trimer were
146 positioned in an "up" conformation, which was similar to the conformation bound to ACE2, and
147 the three RBDs were bound to three Fab molecules. Notably, the C-termini of the three Fabs were
148 positioned close to each other and pointed away from the S protein, suggesting that a single IgG
149 may be able to present two Fabs in a manner that would enable simultaneous engagement of
150 two RBDs on a single S protein. Indeed, this was confirmed in single particle negative stain
151 electron micrographs of IgG 15033 and the S protein, which revealed that the two Fabs of a single
152 IgG bound two RBDs on a single S protein trimer with a pincer-like grip (**Fig. S3B**). Taken together,
153 the X-ray crystallography and electron microscopy showed that Fabs 15033 and 15033-7 block
154 ACE2 binding to RBD by direct steric hinderance, and simultaneous binding of Fabs to multiple
155 RBDs on the S protein trimer enables the IgGs to inhibit ACE2 binding with enhanced potency due
156 to avidity.
157
158 **Engineering of tetravalent nAbs with enhanced avidities**
159 Next, we explored whether we could further enhance the avidity of nAbs by taking
160 advantage of modular design strategies to engineer tetravalent formats. Each SARS-CoV-2
161 particle displays multiple S protein trimers, suggesting that multivalent Fab binding could
162 enhance avidity, especially since a single IgG 15033 molecule can utilize both Fab arms to bind a
163 single S protein trimer. We reasoned that additional Fab arms added to an IgG may further
164 enhance avidity by interacting with RBDs on S protein trimers close to the trimer engaged by the
165 core IgG. Thus, we designed tetravalent versions of 15033 and 15033-7 by fusing additional Fabs
166 to either the N- or C- terminus of the IgG heavy chain to construct molecules termed Fab-IgG or
167 IgG-Fab, respectively (**Fig. 3A**). Consistent with our hypothesis, the tetravalent molecules
168 exhibited higher avidity, and consequently, greatly reduced off rates compared with their
169 bivalent counterparts, and dissociation constants were in the low single-digit picomolar range
170 (**Fig. 3B, Table 1**).
171 Our ultimate aim was to produce therapeutic Abs that could be used to treat COVID-19 in
172 patients. Aside from high affinity and specificity, effective Ab drugs must also possess favorable

173 biophysical properties including high yields from recombinant expression in mammalian cells,
174 high thermodynamic stability, and lack of aggregation and excessive hydrophobic surface area.
175 All IgGs and tetravalent molecules were produced in high yields by transient expression in
176 Expi293F cells (160-200 mg/L, **Table 1**). All proteins were highly thermostable with melting
177 temperatures of the CH3/Fab domain ranging from 81-87 ^{o}C, which exceeded the melting
178 temperature of the trastuzumab Fab (79.5 ^{o}C, **Table 1**). Size exclusion chromatography revealed
179 that all IgGs eluted as a predominant monodisperse single peak with elution volumes nearly
180 identical to that of trastuzumab (**Fig. 3C and Table 1**), and the monomeric fraction was calculated
181 to be 91 to >95% (**Table 1**). All tetravalent molecules also eluted as single peaks in advance of
182 trastuzumab, consistent with their larger molecular weights. IgG and tetravalent versions of both
183 15033 and 15033-7 could be purified to near homogeneity by protein-A affinity chromatography,
184 as evidenced by SDS-PAGE (**Fig. 3D**). Taken together, these analyses demonstrate that the IgGs
185 and their tetravalent derivatives possess good drug-like biophysical properties, which should
186 facilitate drug development at large scale.
187
188 **Inhibition of SARS-CoV-2 infection in cell-based assays**
189 We assessed the effects of the nAbs on virus infection in a neutralization assay that
190 measured the infection of ACE2-expressing Vero E6 cells with the SARS-CoV-2 strain 2019 n-
191 CoV/USA_WA1/2020. All three high affinity nAbs from the naïve library (**Fig. 1**) exhibited dose-
192 dependent neutralization of SARS-CoV-2 infection, confirming their neutralization capacity
193 (**Table 1**). Consistent with affinities, IgG 15033 was most potent with an IC_{50} of 3.5 nM, and its
194 potency was confirmed with the observation of strong neutralization of a second SARS-CoV-2
195 strain (2019-nCoV/Italy-INMI1, data not shown)**.** Moreover, the tetravalent Fab-IgG and IgG-Fab
196 versions of 15033 exhibited improved potencies with IC_{50} values of 320 or 320 pM, respectively
197 (**Fig. 4A and Table 1**). The optimized IgG 15033-7 also exhibited high neutralizing potency with
198 an IC_{50} of 790 pM and its tetravalent Fab-IgG and IgG-Fab versions exhibited the best potencies
199 of all molecules tested with IC_{50} values of 100 or 61 pM, respectively. Taken together, these
200 results showed that naïve synthetic Ab libraries can yield highly potent nAbs with excellent drug-

201 like properties, and further optimization and engineering of tetravalent formats can produce
202 drug-like molecules with ultra-high potencies beyond those of bivalent IgGs.
203
204 **Resistance to potential viral escape mutants**
205 To explore neutralization of potential escape mutants, we generated HIV-gag-based
206 lentivirus-like particle (VLPs) pseudotyped with the SARS-CoV-2 S protein. We confirmed ACE2-
207 dependent uptake of the pseudotyped VLPs by HEK-293 cells stably over-expressing exogenous
208 ACE2, and we showed that uptake was inhibited by either Fc-tagged RBD (RBD-Fc) or IgG 15033.
209 Within this system, we generated a panel of 44 pseudotyped VLP variants, each containing a
210 single alanine substitution at an RBD position within or close to the ACE2-binding site. Twenty of
211 these VLP variants exhibited a >4-fold reduction in internalization compared with the wild-type
212 (wt) VLP, suggesting that these wt side chains contributed favorably to the interaction between
213 the RBD and ACE2. The remaining 24 VLP variants were internalized with high efficiency, and
214 these represent good mimics of escape mutants, which maintain strong ACE2-mediated
215 infectivity but may potentially reduce binding to nAbs that compete directly with ACE2.
216 With the panel of 24 VLP variants that mimicked potential escape mutants, we surveyed
217 the effects on cellular uptake after treatment with various nAbs (**Fig. 4B**). We defined as escape
218 mutants those VLP variants for which cellular uptake in the presence of 50 nM nAb was >5% of
219 the uptake in the absence of the nAb. Based on this definition, we found that 6 of the mutations
220 enabled escape from IgG 15033, whereas only three mutations enabled escape from IgG 15033-
221 7. Presenting the 15033 paratope in tetravalent formats resulted in nAbs that could neutralize
222 more variants than IgG 15033, and most importantly, tetravalent nAbs containing the 15033-7
223 paratope strongly neutralized all variants except one. As expected, these results showed that
224 enhancing the avidity of the IgG paratope for the S protein enhanced both potency and resistance
225 to escape mutations. Moreover, similar enhancements were also achieved by the presentation
226 of paratopes in tetravalent rather than bivalent formats, and the most effective nAbs were those
227 that presented the optimized paratope in the tetravalent format.
228
229

230 **DISCUSSION**

231 SARS-CoV-2 has wreaked havoc on global health and economics, and along with its relatives
232 SARS-CoV and MERS, has shown that viral outbreaks and pandemics will continue to plague the
233 world in the future. Consequently, it is essential for the scientific community to adapt the most
234 advanced drug development technologies to combat not only COVID-19, but also, pathogenic
235 disease in general. In this context, we have deployed advanced synthetic antibody engineering
236 to rapidly develop human nAbs, which are potent therapeutic candidates in the natural IgG
237 format, and are even better neutralizing agents in the synthetic tetravalent formats that our
238 modular design strategies enable. Most importantly, the enhanced affinities and potencies
239 afforded by tetravalent nAbs are achieved without compromising any of the favorable
240 characteristics that make IgG molecules ideal drugs. Moreover, tetravalent nAbs resist potential
241 escape mutants, which further augments the power of these molecules as drugs to combat not
242 only SARS-CoV-2, but also, its relatives that may emerge in the future.

243 COVID-19 has also exposed the need for drug development to respond to viral outbreaks
244 in real time, to prevent the global spread of viral pathogens to the point where a pandemic
245 threatens the entire global community. In this regard, the most rapid method for drug
246 development to combat COVID-19 has proven to be the manufacture of nAbs isolated from
247 infected patients by B cell cloning. Several reports have now shown that these technologies can
248 deliver drug-grade therapeutic nAbs for manufacturing and subsequent clinical trials in
249 approximately six months[17,27]. These extraordinarily rapid drug development timelines set a
250 benchmark for alternative technologies.

251 With our platform, we show that synthetic *in vitro* antibody engineering holds up well
252 against B cell cloning, both in terms of speed and quality of drug development. Our project was
253 initiated at the beginning of April, 2020 when we identified our first naïve Ab leads targeting the
254 SARS-CoV-2 S protein. Within a month, we had validated lead IgG molecules as neutralizing
255 agents in cell-based assays with authentic virus. In parallel, we initiated further selections to
256 optimize the Fab 15033 paratope, which yielded our best lead nAb 15033-7, and we reformatted
257 this lead in to the tetravalent formats that further enhanced potency. By the beginning of
258 October, we had established manufacturing-grade stable cells capable of producing multi-gram

259 quantities of drug-grade nAbs from a litre of culture, in both the IgG and tetravalent formats. We
260 are now manufacturing our best nAb for clinical trials. Thus, we have shown that synthetic Ab
261 engineering technologies can match the six-month lead-to-manufacture timelines established by
262 methods based on cloning of natural nAbs, and further improvements are possible by further
263 streamlining of key development steps.

264 Moreover, synthetic engineering technologies hold key advantages over natural cloning
265 methods. First, synthetic engineering offers exquisite control over Ab design; as we have shown,
266 optimal frameworks and diversity designs can ensure that candidate therapeutics possess
267 biophysical properties that are ideal for drug development. Also, the use of highly stable
268 frameworks facilitates the rapid construction of complex tetravalent formats that enhance
269 potency while retaining favorable drug-like properties. Perhaps most importantly, synthetic
270 methods can overcome a fundamental limitation of technologies that depend on natural
271 repertoires, namely, the need for infected patients as a source of drug leads. By its very nature,
272 B cell cloning is a reactive technology that can only be implemented once a viral outbreak is
273 underway, and this places a fundamental limit on the time required for drug development. With
274 synthetic *in vitro* methods, drug development can proceed in a proactive manner, as
275 development and stockpiling of potential therapeutics in advance of outbreaks is feasible.
276 Indeed, large-scale sequencing efforts have provided unprecedented access to the genomes of
277 thousands of SARS-CoV-2 relatives and other pathogens that may be poised to cause future
278 outbreaks[28,29]. With our methods, we have shown that it is feasible to develop synthetic Abs
279 targeting hundreds of antigens in parallel[30], and thus, it is entirely feasible to target in advance
280 the myriad pathogens that may pose future health risks. Working within a collaborative
281 international network, we have initiated efforts with this aim.
282
283
284

285

286 **METHODS AND MATERIALS**

287 **Cells**

288 Cells were maintained in humidified environments at 37 °C in 5% CO_2 in the indicated media. Vero
289 E6 (ATCC), HEK293T (ATCC) and HEK293T cells stably overexpressing ACE2 were maintained at 37
290 °C in 5% CO_2 in DMEM containing 10% (vol/vol) FBS. Expi293F cells (ThermoFisher) were
291 maintained at 37 °C in 8% CO_2 in Expi293F expression media (ThermoFisher).

292

293 **Protein Production**

294 The previously reported piggyBac transposase-based expression plasmid PB-T-PAF[31] containing a
295 CMV promotor (PB-CMV) and a woodchuck hepatitis virus posttranscriptional regulatory element
296 (WPRE) was used for large-scale transient expression. cDNA encoding the SARS-CoV-2 spike
297 ectodomain trimer (residues 1-1211), followed by a foldon trimerization motif[32], a 6xHis tag and
298 an AviTag biotinylation motif[33] was cloned in to the PB-CMV vector using standard molecular
299 biology techniques and residues 682–685 (RRAR) and 986–987 (KV) were mutated to SSAS and
300 two proline residues to remove the furin cleavage site on the SARS-CoV-2 spike protein and
301 stabilize the pre-fusion form of the spike[34], respectively. The SARS-CoV-2 receptor binding
302 domain (RBD, residues 328-528), the soluble human ACE2 construct (residues 19-615), and the
303 SARS-CoV RBD (residues 315-514), each followed by a 6xHis tag and an AviTag, were similarly
304 cloned in to the same vector. For expression, PB-CMV expression constructs were mixed with
305 Opti-MEM media (Gibco) containing 293fectin reagent (Thermo Fisher) and the mixture
306 incubated for 5 min before addition to the shaker flask containing 10^6 Freestyle 293-F cells/mL
307 grown in suspension in Freestyle 293 expression media (Thermo Fisher). Expression was allowed
308 to continue for 6 days before purification.

309

310 **Protein purification and *in vitro* biotinylation**

311 Expressed proteins were harvested from expression medium by binding to Ni-NTA affinity resin
312 eluted with 1X PBS containing 300 mM imidazole and 0.1% (v/v) protease inhibitor cocktail
313 (Sigma), then further purified by size-exclusion chromatography. For the RBDs and ACE2, a

314 Superdex 200 Increase (GE healthcare) column was used. For the spike ectodomain, a Superose
315 6 Increase (GE healthcare) column was used. Purified proteins were site-specifically biotinylated
316 in a reaction with 200 µM biotin, 500 µM ATP, 500 µM $MgCl_2$, 30 µg/mL BirA, 0.1% (v/v) protease
317 inhibitor cocktail and not more than 100 µM of the protein-AviTag substrate. The reactions were
318 incubated at 30 °C for 2 hours and biotinylated proteins then purified by size-exclusion
319 chromatography.
320
321 **Phage panning**
322 A validated, synthetic, phage-displayed antibody library[24] was panned on SARS-CoV-2 spike RBD
323 in solution. In each round, phage library was first depleted on neutravidin immobilized in wells
324 of a 96 Maxisorp plate from a 2 µg/mL solution incubated with shaking overnight at 4 °C, then
325 incubated with 50 nM biotinylated RBD in solution for two hours at RT. Protein-phage complexes
326 were captured in wells coated with neutravidin as above for 15 min at RT, then washed with 1X
327 PBS pH7.4 containing 0.05% Tween and phage eluted for 5 min with 0.1 M HCl before neutralizing
328 with 1M Tris pH 8.0. Eluted phage were amplified, purified, then panned against target for a total
329 of 5 rounds, before isolation, amplification and sequencing of individual phage clones as
330 previously described[24].
331
332 **Enzyme linked immunosorbent assays**
333 For ELISAs, plates were coated with neutravidin, as above, then blocked with 0.2% BSA in PBS for
334 1 hr. Biotinylated target protein was captured from solution by incubation in neutravidin-coated
335 and BSA-blocked wells for 15 min with shaking at RT before addition and 30 min incubation of
336 binding phage or antibody. Plates were washed then incubated with an appropriate secondary
337 antibody before development with TB substrate as described[35].
338
339 **Tetravalent Antibody Construction**
340 DNA fragments encoding heavy chain Fab regions (VH-CH1; terminating at threonine 238,
341 Kabat numbering) were amplified by PCR from the IgG expression constructs. Tetravalent
342 antibody constructs were generated by fusing these fragments with their respective IgG heavy

343 chain in the pSCSTa mammalian expression vector using Gibson assembly (NEB). Fab-IgG
344 constructs were arranged by fusing a heavy chain Fab domain to the N-terminus of the IgG via a
345 $S(G4S)_3$ linker. IgG-Fab constructs were arranged by fusing a heavy chain Fab domain to the C-
346 terminus using a $G(G4S)_2GGGTG$ linker. For both formats, the Fc region terminated at glycine 447
347 (Kabat numbering).
348
349 **Antibody Production**
350 IgG and tetravalent antibodies were produced in Expi293F (ThermoFisher) by transient
351 transfection, by diluting heavy and light chain construct DNA in OptiMem serum-free media
352 (Gibco) before the addition of and incubation with FectoPro (Polyplus Transfection) for 10 min.
353 For IgG expression, equivalent amounts of plasmids encoding heavy chain and light chains were
354 transfected, whereas for tetravalent modalities, a ratio of 2:1 light chain to heavy chain plasmids
355 was used. Following addition of the DNA complex to Expi293F cell and a 5-day expression period,
356 antibodies were purified using rProtein A Sepharose (GE Healthcare), then buffer exchanged and
357 concentrated using Amicon Ultra-15 Centrifugal Filter devices (Millipore). IgGs were stored in PBS
358 (Gibco), while tetravalent antibodies were stored in a 10 mM L-Histidine, 0.9% sucrose, 140 mM
359 NaCl, pH 6.0 buffer.
360
361 **Size-exclusion chromatography**
362 Fifty micrograms of protein were injected onto a TSKgel BioAssist G3SWxl (Tosoh) fitted with a
363 guard column using an NGC chromatography system and a C96 autosampler (Biorad). The column
364 was preequilibrated in a PBS mobile phase and protein retention was monitored by absorbance
365 at 215 nm during a 1.5 CV isocratic elution in PBS.
366
367 **Biolayer interferometry**
368 The binding kinetics and estimation of apparent affinity (K_D) of antibodies against SARS CoV-2
369 spike RBD were determined by biolayer interferometry experiments performed on an Octet HTX
370 instrument (ForteBio) at 1000 rpm and 25 ^{o}C. Biotinylated CoV-2 spike protein was first captured
371 on streptavidin biosensors from a 2 μg/mL solution to achieve a binding response of 0.4-0.6 nm
372 and unoccupied sites quenched with 100 μg/mL biotin. Antibodies were diluted with assay buffer

373 (PBS, 1% BSA, 0.05% Tween 20) and 67 nM of an unrelated biotinylated protein of similar size
374 was used as negative control. Following equilibration with assay buffer, loaded biosensors were
375 dipped for 600 s into wells containing 3-fold serial dilutions of each antibody from 67 nM and
376 subsequently were transferred for 600 s back into assay buffer. Binding response data were
377 reference subtracted and were fitted with 1:1 binding model using ForteBio's Octet Systems
378 software 9.0.
379
380 **Differential scanning fluorimetry**
381 Thermostability of expressed antibodies were determined by differential scanning fluorimetry
382 (DSF) using Sypro Orange as described[36] instead using a 1 μM solution of antibody and
383 temperature range from 25-100 ºC in 0.5º increments.
384
385 **Generation of SARS-CoV-2 pseudovirus**
386 To generate SARS-CoV-2 pseudovirus, human embryonic kidney 293 (HEK 293)(ATCC) cells were
387 seeded in a 6-well plate at $0.3x10^6$ cells/well in DMEM (ThermoFisher) supplemented with 10%
388 FBS and 1% penicillin-streptomycin (Gibco) and grown overnight at 37 °C, 5% CO_2. HEK 293 cells
389 were then co-transfected with 1 μg of pNL4-3.luc.R-E- plasmid (luciferase expressing HIV-1 with
390 defective envelop protein) (NIH AIDS Reagent Program) and 0.06 μg of CMV-promoter driven
391 plasmid encoding SARS-CoV-2 wild type or mutant spike variants using Lipofectamine™ 2000
392 transfection reagent (ThermoFisher). Pseudovirus was harvested by collecting supernatant 48 h
393 after transfection and filter sterilized (0.44 μm, Millipore Sigma, Cat. No. SLHA033SS).
394
395
396 **Pseudovirus Entry Assay**
397 HEK 293 cells (ATCC) stably over-expressing full-length human ACE2 protein were seeded in 96
398 well white polystyrene microplates (Corning, Cat. No. CLS3610) at $0.03x10^6$ cells/well in DMEM
399 (10% FBS and 1% Pen-Strep), and grown overnight at 37 °C, 5% CO_2. To test the inhibition of
400 pseudovirus entry of antibodies, the desired concentrations of antibodies were mixed with
401 pseudoviruses, incubated at room temperature for 10 min, and were used to infect cells. The
402 cells were incubated at 37 °C, 5% CO_2 for 6 h, then the medium was replaced with fresh DMEM

403 (10% FBS and 1% Pen-Strep), and again every 24 h up to 72 h. To measure the luciferase signal
404 (virus uptake), DMEM was removed and cells were replaced in DPBS (ThermoFisher) and mixed
405 with an equal volume of ONE-Glo™ EX Luciferase Assay System (Promega). Relative luciferase
406 units were measured using a BioTek Synergy Neo plate reader (BioTek Instruments Inc.). The data
407 was then analyzed by GraphPad Prism Version 8.4.3 (GraphPad Software, LLC.).
408
409 **SARS-CoV-2 focal reduction neutralization assay**
410 SARS-CoV-2 strain 2019 n-CoV/USA_WA1/2020 was obtained from the Centers for Disease
411 Control (USA) and Prevention (gift of Natalie Thornburg). Virus stocks were produced in Vero
412 CCL81 cells (ATCC) and titrated by focus-forming assay on Vero E6 cells[37]. Serial dilutions of mAbs
413 were incubated with 10^2 focus-forming units (FFU) of SARS-CoV-2 for 1 h at 37°C. MAb-virus
414 complexes were added to Vero E6 cell monolayers in 96-well plates and incubated at 37°C for 1
415 h. Subsequently, cells were overlaid with 1% (w/v) methylcellulose in MEM supplemented with
416 2% FBS. Plates were harvested 30 h later by removing overlays and fixed with 4% PFA in PBS for
417 20 min at room temperature. Plates were washed and sequentially incubated with 1 µg/mL of
418 CR3022[38] anti-S antibody and HRP-conjugated goat anti-human IgG in PBS supplemented with
419 0.1% saponin and 0.1% BSA. SARS-CoV-2-infected cell foci were visualized using TrueBlue
420 peroxidase substrate (KPL) and quantitated on an ImmunoSpot microanalyzer (Cellular
421 Technologies). Data were processed using Prism software (GraphPad Prism 8.0).
422
423 **SARS-CoV-2 micro neutralization assay**
424 SARS-CoV-2 strain 2019-nCoV/Italy-INMI1 was obtained from the National Institute for Infectious
425 Diseases Lazzaro Spallanzani IRCCS (Italy) and passaged in Vero E6 cells[39] before determining the
426 tissue culture infectious dose (TCID50) as described[40]. Antibodies were serially diluted two-fold
427 in serum-free medium and mixed with an equal volume of 100X the TCID50/well SARS-CoV-2
428 virus then incubated at 37°C for 30 min. Sub-confluent Vero E6 cell monolayers in tissue culture
429 plates were infected with virus-serum mixtures in duplicate and incubated at 37°C in % CO2 for
430 two days. The supernatant of each plate was then carefully discarded and cell viability

431 determined by crystal violet assay reading the absorbance at 595 nm (Synergy HTX Biotek) as
432 described[41].
433
434 **X-ray crystallography**
435 For the x-ray crystallographic work, the SARS-CoV-2 RBD (residues 328-528) was expressed with
436 a C-terminal 6xHis tag from HEK293F GnT1-minus cells. The Fabs were expressed from HEK293F
437 cells. The RBD was purified from the expression media by metal-affinity chromatography using
438 Ni-NTA beads (Qiagen). The Fabs were purified from the expression media using rProtein A
439 Sepharose Fast Flow beads (GE healthcare). The RBD was treated with endoglycosidase H[42] and
440 Carboxypeptidase A (Sigma-Aldrich), to remove the N-glycans and the C-terminal 6xHis tag. The
441 RBD and Fabs were then further purified by ion-exchange and hydrophobic interaction
442 chromatography. Before crystallization, the RBD-Fab complexes were purified using size-
443 exclusion chromatography on a Superdex 200 Increase column (GE Healthcare). For both Fab
444 15033 and Fab 15033-7, the optimized crystallization conditions contained 1.2-1.6 M $(NH_4)_2SO_4$
445 and 8-18% glycerol. X-ray diffraction data were collected at 100 K on beamline 08IB-1 at the
446 Canadian Light Source. The diffraction data were integrated and scaled using the XDS package[43].
447 The structures were solved by molecular replacement using the program Phaser[44]. A homology
448 model of the VH-VL region was produced by the SysImm Repertoire Builder server
449 (https://sysimm.org/rep_builder,
450 https://pubs.rsc.org/en/content/articlehtml/2019/me/c9me00020h). The CDR loops were then
451 deleted from this VH-VL model. The constant (CH1-CL) region search model and the RBD search
452 model were both derived from PDB entry 6W41[38]. The three models were used to solve the
453 structure my molecular replacement. The atomic models were built using Coot[45] and refined with
454 Phenix.refine[46].
455
456
457

458 **FIGURES**

459 **Figure 1. Characterization of anti-RBD Abs by ELISA.**

460 **Figure 1**

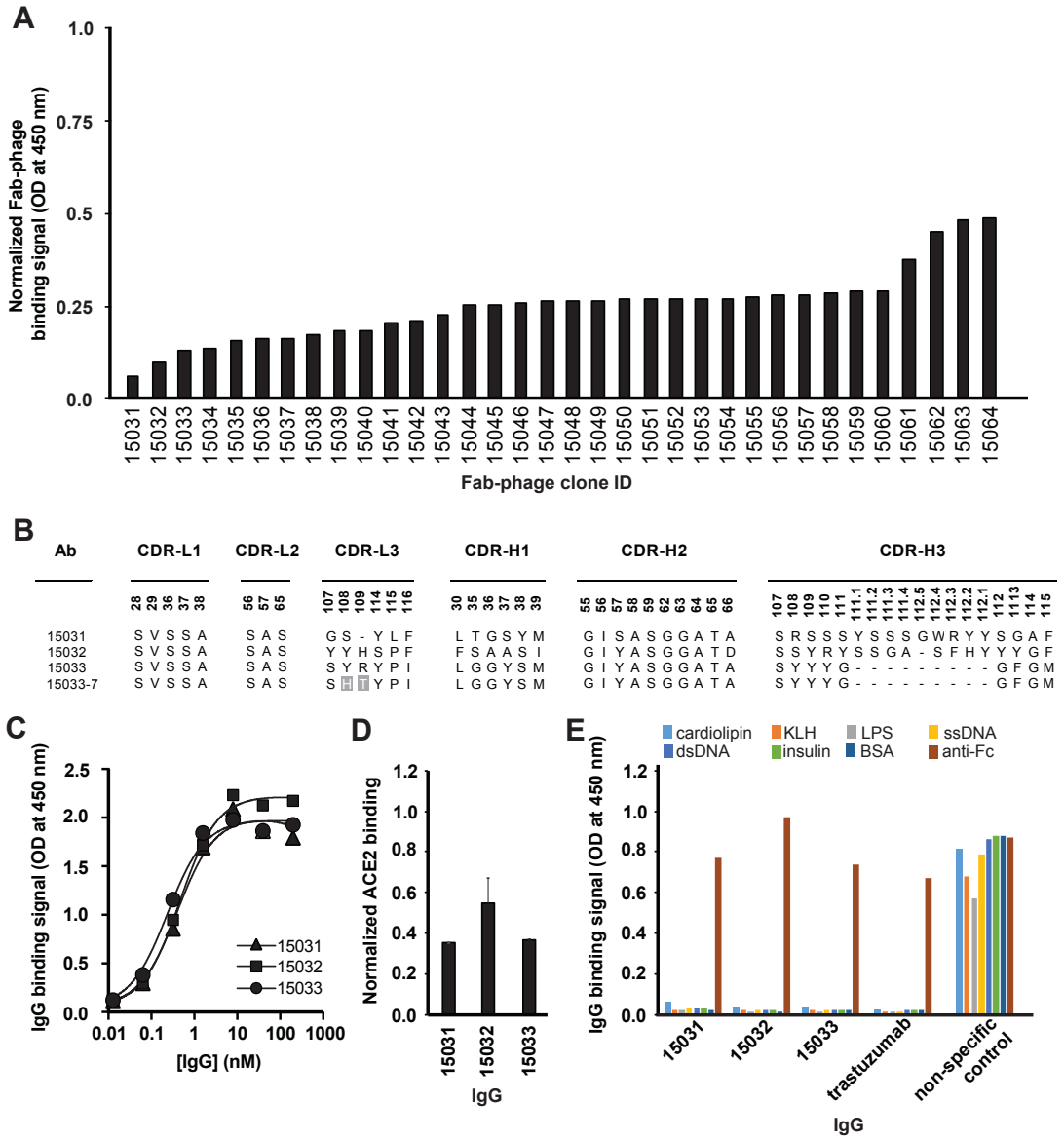

481 **Figure 1. Characterization of anti-RBD Abs by ELISA. (A)** Binding of unique Fab-phage
482 clones (x-axis) to immobilized RBD blocked by solution-phase ACE2 (y-axis). Signal was
normalized to the signal in the absence of ACE2. **(B)** CDR sequences of Abs for which
483 the binding to RBD was strongly blocked by ACE2. Positions that are highly variable in
the immune repertoire are shown and are numbered according to the IMGT
484 nomenclature[47]. Sequences in 15033-7 that differ from 15033 are shaded *grey.* **(C)**
Serial dilutions of IgGs (x-axis) binding to immobilized S protein trimer (y-axis). The
485 EC_{50} values derived from the curves are shown in Table 1 and values are representative
of 2 independent experiments. **(D)** Binding of biotinylated ACE2 (y-axis) to immobilized
486 S protein blocked by solution-phase IgG (x-axis). Signal was normalized to the signal in
the presence of a non-binding control IgG and error bars shown as the standard error
of the mean of duplicate samples. (**E**) Assessment of non-specific binding (y-axis) of
IgGs (x-axis) to immobilized antigens or a goat anti-human Fc Ab (positive control).

487 **Figure 2. Structural analysis of Fabs bound to the RBD.**

488 Figure 2

489 A B

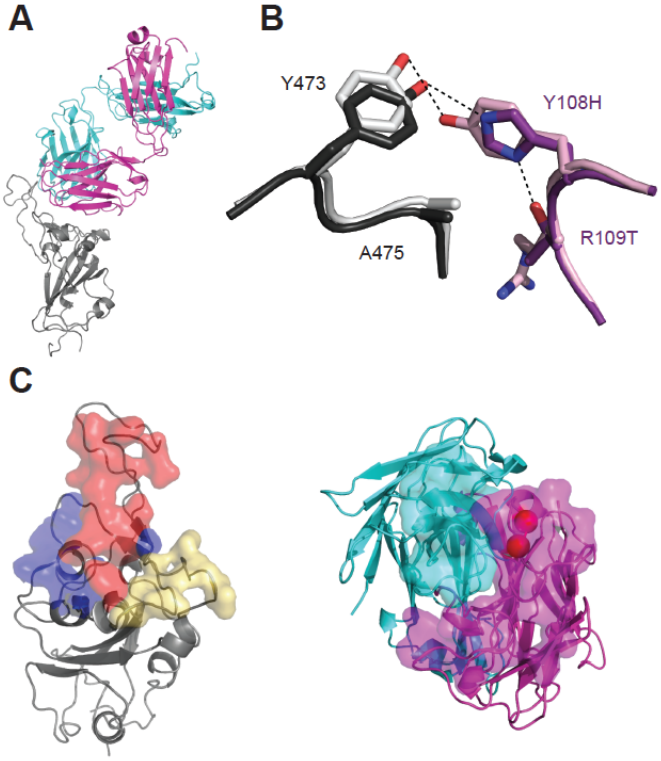

502 **Figure 2. Structural analysis of Fabs bound to the RBD. (A)** The crystal structure of
503 Fab 15033-7 (light chain, magenta; heavy chain, cyan) in complex with the SARS-
504 CoV-2 RBD (grey). **(B)** Side chain interactions between CDR-L3 residues and the RBD.
505 Superposed CDR-L3 loops of Fabs 15033 and 15033-7 are colored light or dark
506 purple, respectively, and the RBD residues they contact are colored light or dark
507 grey, respectively. CDR-L3 residues are numbered with the sequence in Fab 15033
508 or 15033-7 to the left or right of the number, respectively. Hydrogen bonds are
509 indicated by dashed lines. (**C**) The structural epitope and paratope. The RBD (left)
510 and Fab 15033-7 (right) are shown in an open book view and residues within 4.0 Å
511 of the cognate ligand are shown as colored surfaces. For the RBD, residues in the
512 ACE2-binding site are also shown as colored surfaces, and the following color
513 scheme was used: red, contacts with both Fab 15033-7 and ACE2; blue, contacts
514 with Fab 15033-7 only; yellow, contacts with ACE2 only. Fab 15033-7 residues that
515 contact the RBD are colored magenta or cyan if they reside in the light or heavy
chain, respectively. The CDR-L3 residues that differ between 15033-7 and 15033 are
shown as red spheres.

516 **Figure 3. Design and characterization of tetravalent nAbs.**

517
518
519
520
521
522
523
524
525
526
527
528
529
530
531
532
533
534
535
536
537
538
539

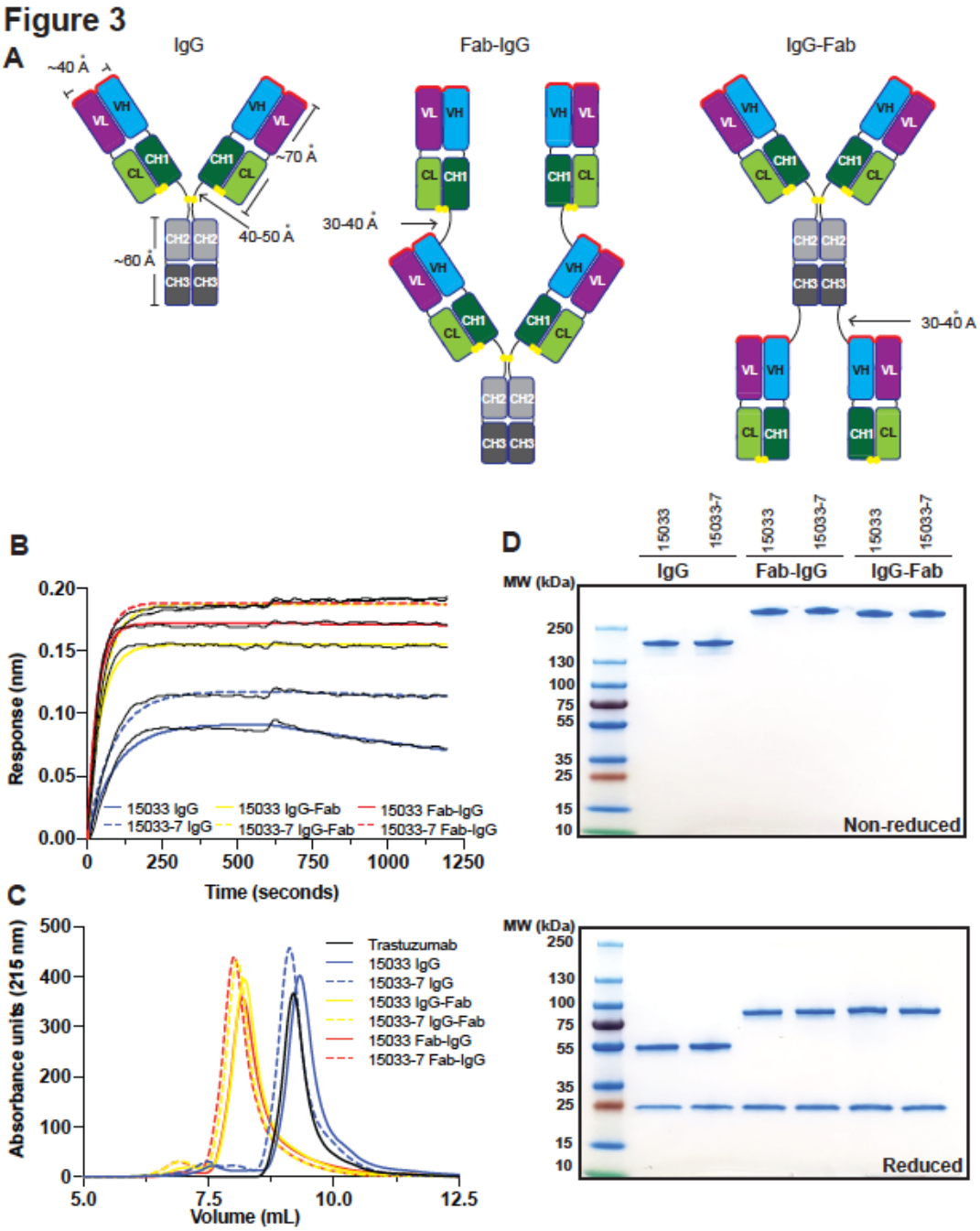

540 **Figure 3. Design and characterization of tetravalent nAbs. (A)** Schematic of the
541 bivalent IgG format, and the tetravalent Fab-IgG and IgG-Fab formats. Paratopes
542 are shown in red, linkers are shown in black, and disulfide bonds are shown as
543 yellow spheres. **(B)** BLI sensor traces for nAbs binding to immobilized S protein
544 trimer. **(C)** Analytical gel filtration of nAbs. **(D)** SDS-PAGE analysis of nAbs under non-reducing (top) or reducing conditions (bottom) and are representative of n=2 independent preparations.

Figure 4. Neutralization of SARS-CoV-2 virus and pseudotyped VLPs.

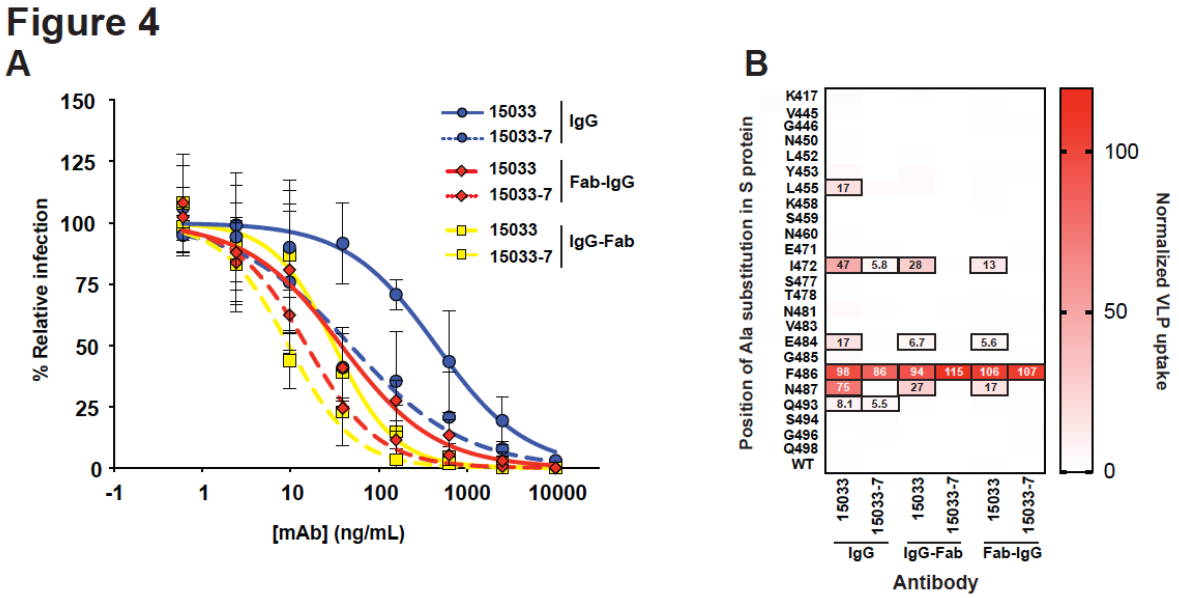

Figure 4. Neutralization of SARS-CoV-2 virus and pseudotyped VLPs. (A) Neutralization of SARS-CoV-2 strain 2019 n-CoV/USA_WA1/2020 by bivalent and tetravalent nAbs. The virus was pre-treated with serial dilutions of nAb (x-axis) and infection of ACE2-expressing Vero E6 cells was measured relative to untreated control (y-axis). Samples were run in duplicate and results and are representative of n=2 independent experiments. Error bars indicate standard error of the mean. **(B)** Neutralization of a panel of pseudotyped VLPs displaying SARS-CoV-2 S proteins with single alanine mutations in or near the ACE2-binding site (y-axis). The VLPs were treated with 50 nM of the indicated nAb (x-axis) and uptake by ACE2-expressing HEK-293 cells was measured in triplicate and results are representative of n=2 independent experiments. The heat map shows uptake normalized to uptake in the absence of nAb. Boxed cells indicate VLPs that represented escape mutants for a given nAb, as defined by >5% uptake with nAb treatment compared with untreated control (the percent uptake is shown in each cell).

573 **Table 1. Characteristics of lead IgG and tetravalent antibodies**

574

575

576

577

578

ID	Format	Yield ($mg \cdot L^{-1}$)	EC_{50} (nM)	k_{on} ($10^5 M^{-1}s^{-1}$)	k_{off} ($10^{-5}s^{-1}$)	Apparent K_D (pM)	Viral IC_{50} ($ng \cdot mL^{-1}$)	Viral IC_{50} (pM)	Spike VLP EC_{50} (nM)	SEC Elution volume (mL)	Mono-dispersity (%)	Tm2 (°C)
trastuzumab	IgG	303	NA	NA	NA	NA	NA	NA	NA	9.20	>95	79.5
15033	IgG	207	0.24	17	50	300	523	3540	0.44	9.34	91	81
15033-7	IgG	165	0.09	18	7	39	118	790	0.37	9.13	95	81
15033	Fab-IgG	214	0.18	46	1.5	3	48	320	0.27	8.22	>95	87
15033-7	Fab-IgG	194	0.14	40	0.8	2	15	100	0.35	8.02	93	85.5
15033	IgG-Fab	166	0.11	36	1.9	5	51	340	0.27	8.22	>95	87
15033-7	IgG-Fab	118	0.15	30	<0.1	<1	9.1	61	0.47	8.09	93	85

579

580

581

582

583

584

585

586

587

588

589

590

591

592

593

594

595

596

597

598

599

600

601

602

603 **REFERENCES**

604 1. Beigel JH, Tomashek KM, Dodd LE, Mehta AK, Zingman BS, Kalil AC, Hohmann E, Chu HY,
605 Luetkemeyer A, Kline S, et al. Remdesivir for the Treatment of Covid-19 — Preliminary
606 Report. N Engl J Med 2020;
607 2. Boulware DR, Pullen MF, Bangdiwala AS, Pastick KA, Lofgren SM, Okafor EC, Skipper CP,
608 Nascene AA, Nicol MR, Abassi M, et al. A Randomized Trial of Hydroxychloroquine as
609 Postexposure Prophylaxis for Covid-19. N Engl J Med 2020; 383:517–25.
610 3. Robbiani DF, Gaebler C, Muecksch F, Lorenzi JCC, Wang Z, Cho A, Agudelo M, Barnes CO,
611 Gazumyan A, Finkin S, et al. Convergent antibody responses to SARS-CoV-2 in
612 convalescent individuals. Nature 2020; 584:437–42.
613 4. Long QX, Tang XJ, Shi QL, Li Q, Deng HJ, Yuan J, Hu JL, Xu W, Zhang Y, Lv FJ, et al. Clinical
614 and immunological assessment of asymptomatic SARS-CoV-2 infections. Nat Med 2020;
615 26:1200–4.
616 5. Li L, Zhang W, Hu Y, Tong X, Zheng S, Yang J, Kong Y, Ren L, Wei Q, Mei H, et al. Effect of
617 Convalescent Plasma Therapy on Time to Clinical Improvement in Patients With Severe
618 and Life-threatening COVID-19: A Randomized Clinical Trial. JAMA 2020;
619 6. Shen C, Wang Z, Zhao F, Yang Y, Li J, Yuan J, Wang F, Li D, Yang M, Xing L, et al. Treatment
620 of 5 Critically Ill Patients with COVID-19 with Convalescent Plasma. JAMA - J Am Med
621 Assoc 2020; 323:1582–9.
622 7. Duan K, Liu B, Li C, Zhang H, Yu T, Qu J, Zhou M, Chen L, Meng S, Hu Y, et al. Effectiveness
623 of convalescent plasma therapy in severe COVID-19 patients. Proc Natl Acad Sci U S A
624 2020; 117:9490–6.
625 8. Alsoussi WB, Turner JS, Case JB, Zhao H, Schmitz AJ, Zhou JQ, Chen RE, Lei T, Rizk AA,
626 McIntire KM, et al. A Potently Neutralizing Antibody Protects Mice against SARS-CoV-2
627 Infection. J Immunol 2020; 205:915–22.
628 9. Shi R, Shan C, Duan X, Chen Z, Liu P, Song J, Song T, Bi X, Han C, Wu L, et al. A human
629 neutralizing antibody targets the receptor-binding site of SARS-CoV-2. Nature 2020;
630 584:120–4.
631 10. Sui J, Li W, Murakami A, Tamin A, Matthews LJ, Wong SK, Moore MJ, Tallarico ASC,

632 Olurinde M, Choe H, et al. Potent neutralization of severe acute respiratory syndrome
633 (SARS) coronavirus by a human mAb to S1 protein that blocks receptor association. Proc
634 Natl Acad Sci U S A 2004; 101:2536–41.
635 11. Zhu Z, Chakraborti S, He Y, Roberts A, Sheahan T, Xiao D, Hensley LE, Prabakaran P, Rockx
636 B, Sidorov IA, et al. Potent cross-reactive neutralization of SARS coronavirus isolates by
637 human monoclonal antibodies. Proc Natl Acad Sci U S A 2007; 104:12123–8.
638 12. Meulen J Ter, Bakker ABH, Brink EN Van Den, Weverling GJ, Martina BEE, Haagmans BL,
639 Kuiken T, Kruif J De, Preiser W, Spaan W, et al. Human monoclonal antibody as
640 prophylaxis for SARS coronavirus infection in ferrets. Lancet 2004; 363:2139–41.
641 13. Corti D, Zhao J, Pedotti M, Simonelli L, Agnihothram S, Fett C, Fernandez-Rodriguez B,
642 Foglierini M, Agatic G, Vanzetta F, et al. Prophylactic and postexposure efficacy of a
643 potent human monoclonal antibody against MERS coronavirus. Proc Natl Acad Sci U S A
644 2015; 112:10473–8.
645 14. Klein S, Cortese M, Winter SL, Wachsmuth-Melm M, Neufeldt CJ, Cerikan B, Stanifer ML,
646 Boulant S, Bartenschlager R, Chlanda P. SARS-CoV-2 structure and replication
647 characterized by in situ cryo-electron tomography. bioRxiv 2020; :2020.06.23.167064.
648 15. Ke Z, Oton J, Qu K, Cortese M, Zila V, McKeane L, Nakane T, Zivanov J, Neufeldt CJ,
649 Cerikan B, et al. Structures and distributions of SARS-CoV-2 spike proteins on intact
650 virions. Nature 2020; :1–7.
651 16. Hoffmann M, Kleine-Weber H, Schroeder S, Mü MA, Drosten C, Pö S. SARS-CoV-2 Cell
652 Entry Depends on ACE2 and TMPRSS2 and Is Blocked by a Clinically Proven Protease
653 Inhibitor. Cell 2020; 181:271-280.e8.
654 17. Hansen J, Baum A, Pascal KE, Russo V, Giordano S, Wloga E, Fulton BO, Yan Y, Koon K,
655 Patel K, et al. Studies in humanized mice and convalescent humans yield a SARS-CoV-2
656 antibody cocktail. Science 2020; 369:1010–4.
657 18. Pinto D, Park Y-J, Beltramello M, Walls AC, Tortorici MA, Bianchi S, Jaconi S, Culap K,
658 Zatta F, Marco A De, et al. Cross-neutralization of SARS-CoV-2 by a human monoclonal
659 SARS-CoV antibody.
660 19. Cao Y, Su B, Guo X, Sun W, Deng Y, Bao L, Zhu Q, Zhang X, Zheng Y, Geng C, et al. Potent

661 Neutralizing Antibodies against SARS-CoV-2 Identified by High-Throughput Single-Cell
662 Sequencing of Convalescent Patients' B Cells. Cell 2020; 182:73-84.e16.
663 20. Rogers TF, Zhao F, Huang D, Beutler N, Burns A, He WT, Limbo O, Smith C, Song G, Woehl
664 J, et al. Isolation of potent SARS-CoV-2 neutralizing antibodies and protection from
665 disease in a small animal model. Science (80-) 2020; 369:956–63.
666 21. Wan J, Xing S, Ding L, Wang Y, Gu C, Wu Y, Rong B, Li C, Wang S, Chen K, et al. Human-
667 IgG-Neutralizing Monoclonal Antibodies Block the SARS-CoV-2 Infection. Cell Rep 2020;
668 32.
669 22. Noy-Porat T, Makdasi E, Alcalay R, Mechaly A, Levy Y, Bercovich-Kinori A, Zauberman A,
670 Tamir H, Yahalom-Ronen Y, Israeli M, et al. A panel of human neutralizing mAbs targeting
671 SARS-CoV-2 spike at multiple epitopes. Nat Commun 2020; 11:1–7.
672 23. Wec AZ, Wrapp D, Herbert AS, Maurer DP, Haslwanter D, Sakharkar M, Jangra RK,
673 Dieterle ME, Lilov A, Huang D, et al. Broad neutralization of SARS-related viruses by
674 human monoclonal antibodies. Science (80-) 2020; 369:731–6.
675 24. Persson H, Ye W, Wernimont A, Adams JJ, Koide A, Koide S, Lam R, Sidhu SS. CDR-H3
676 diversity is not required for antigen recognition by synthetic antibodies. J Mol Biol 2013;
677 425:803–11.
678 25. Mouquet H, Scheid JF, Zoller MJ, Krogsgaard M, Ott RG, Shukair S, Artyomov MN,
679 Pietzsch J, Connors M, Pereyra F, et al. Polyreactivity increases the apparent affinity of
680 anti-HIV antibodies by heteroligation. Nature 2010; 467:591–5.
681 26. Jain T, Sun T, Durand S, Hall A, Houston NR, Nett JH, Sharkey B, Bobrowicz B, Caffry I, Yu
682 Y, et al. Biophysical properties of the clinical-stage antibody landscape. Proc Natl Acad Sci
683 U S A 2017; 114:944–9.
684 27. Jones BE, Brown-Augsburger PL, Corbett KS, Westendorf K, Davies J, Cujec TP, Wiethoff
685 CM, Blackbourne JL, Heinz BA, Foster D, et al. Title: LY-CoV555, a rapidly isolated potent
686 neutralizing antibody, provides protection in a non-human primate model of SARS-CoV-2
687 infection.
688 28. Daszak P, Olival KJ, Li H. A strategy to prevent future epidemics similar to the 2019-nCoV
689 outbreak. Biosaf Heal 2020; 2:6–8.

690 29. Shi Z, Hu Z. A review of studies on animal reservoirs of the SARS coronavirus. Virus Res
691 2008; 133:74–87.
692 30. Hornsby M, Paduch M, Miersch S, Sääf A, Matsuguchi T, Lee B, Wypisniak K, Doak A, King
693 D, Usatyuk S, et al. A high through-put platform for recombinant antibodies to folded
694 proteins. Mol Cell Proteomics 2015; 14:2833–47.
695 31. Li Z, Michael IP, Zhou D, Nagy A, Rini JM. Simple piggyBac transposon-based mammalian
696 cell expression system for inducible protein production. Proc Natl Acad Sci U S A 2013;
697 110:5004–9.
698 32. Tao Y, Strelkov S V, Mesyanzhinov V V, Rossmann MG. Structure of bacteriophage T4
699 fibritin: a segmented coiled coil and the role of the C-terminal domain. Structure 1997;
700 5:789–98.
701 33. Fairhead M, Howarth M. Site-specific biotinylation of purified proteins using BirA.
702 Methods Mol Biol 2015; 1266:171–84.
703 34. Pallesen J, Wang N, Corbett KS, Wrapp D, Kirchdoerfer RN, Turner HL, Cottrell CA, Becker
704 MM, Wang L, Shi W, et al. Immunogenicity and structures of a rationally designed
705 prefusion MERS-CoV spike antigen. Proc Natl Acad Sci U S A 2017; 114:E7348–57.
706 35. Miersch S, Maruthachalam BV, Geyer CR, Sidhu SS. Structure-Directed and Tailored
707 Diversity Synthetic Antibody Libraries Yield Novel Anti-EGFR Antagonists. ACS Chem Biol
708 2017; 12:1381–9.
709 36. Niedziela-Majka A, Kan E, Weissburg P, Mehra U, Sellers S, Sakowicz R. High-throughput
710 screening of formulations to optimize the thermal stability of a therapeutic monoclonal
711 antibody. J Biomol Screen 2015; 20:552–9.
712 37. Case JB, Rothlauf PW, Chen RE, Liu Z, Zhao H, Kim AS, Bloyet LM, Zeng Q, Tahan S, Droit L,
713 et al. Neutralizing Antibody and Soluble ACE2 Inhibition of a Replication-Competent VSV-
714 SARS-CoV-2 and a Clinical Isolate of SARS-CoV-2. Cell Host Microbe 2020; 28:475-485.e5.
715 38. Yuan M, Wu NC, Zhu X, Lee CCD, So RTY, Lv H, Mok CKP, Wilson IA. A highly conserved
716 cryptic epitope in the receptor binding domains of SARS-CoV-2 and SARS-CoV. Science
717 2020; 368:630–3.
718 39. Capobianchi MR, Rueca M, Messina F, Giombini E, Carletti F, Colavita F, Castilletti C, Lalle

719 E, Bordi L, Vairo F, et al. Molecular characterization of SARS-CoV-2 from the first case of
720 COVID-19 in Italy. Clin. Microbiol. Infect.2020; 26:954–6.
721 40. A simple method of estimating fifty percent endpoints – ScienceOpen [Internet]. [cited
722 2020 Oct 29]; Available from: https://www.scienceopen.com/document?vid=21401620-
723 94ad-4100-a3e1-56741c541ab6
724 41. Feoktistova M, Geserick P, Leverkus M. Crystal violet assay for determining viability of
725 cultured cells. Cold Spring Harb Protoc 2016; 2016:343–6.
726 42. Primary structure of the Streptomyces enzyme endo-beta-N-acetylglucosaminidase H -
727 PubMed [Internet]. [cited 2020 Oct 30]; Available from:
728 https://pubmed.ncbi.nlm.nih.gov/6429133/
729 43. Kabsch W. XDS. Acta Crystallogr D Biol Crystallogr 2010; 66:125–32.
730 44. McCoy AJ, Grosse-Kunstleve RW, Adams PD, Winn MD, Storoni LC, Read RJ. Phaser
731 crystallographic software. J Appl Crystallogr 2007; 40:658–74.
732 45. Emsley P, Lohkamp B, Scott WG, Cowtan K. Features and development of Coot. Acta
733 Crystallogr Sect D Biol Crystallogr 2010; 66:486–501.
734 46. Afonine P V., Grosse-Kunstleve RW, Echols N, Headd JJ, Mo
735 riarty NW, Mustyakimov M, Terwilliger TC, Urzhumtsev A, Zwart PH, Adams PD. Towards
736 automated crystallographic structure refinement with phenix.refine. Acta Crystallogr
737 Sect D Biol Crystallogr 2012; 68:352–67.
738 47. Lefranc MP, Pommié C, Ruiz M, Giudicelli V, Foulquier E, Truong L, Thouvenin-Contet V,
739 Lefranc G. IMGT unique numbering for immunoglobulin and T cell receptor variable
740 domains and Ig superfamily V-like domains. Dev Comp Immunol 2003; 27:55–77.
741
742
743
744
745

746